Zhao *et al.*
Chinese Journal of Mechanical Engineering (2024) 37:20
https://doi.org/10.1186/s10033-024-00997-8

Chinese Journal of Mechanical Engineering

ORIGINAL ARTICLE

Open Access

Integrated Active Suspension and Anti-Lock Braking Control for Four-Wheel-Independent-Drive Electric Vehicles

Ze Zhao[1], Lei Zhang[1*], Xiaoling Ding[1], Zhiqiang Zhang[1], Shaohua Li[2*] and Liang Gu[1]

Abstract

This paper presents an integrated control scheme for enhancing the ride comfort and handling performance of a four-wheel-independent-drive electric vehicle through the coordination of active suspension system (ASS) and anti-lock braking system (ABS). First, a longitudinal-vertical coupled vehicle dynamics model is established by integrating a road input model. Then the coupling mechanisms between longitudinal and vertical vehicle dynamics are analyzed. An ASS-ABS integrated control system is proposed, utilizing an H_∞ controller for ASS to optimize load transfer effect and a neural network sliding mode control for ABS implementation. Finally, the effectiveness of the proposed control scheme is evaluated through comprehensive tests conducted on a hardware-in-loop (HIL) test platform. The HIL test results demonstrate that the proposed control scheme can significantly improve the braking performance and ride comfort compared to conventional ABS control methods.

Keywords Four-wheel-independent-drive electric vehicles, Active suspension system (ASS), Anti-lock braking system (ABS), Vertical-longitudinal vehicle dynamics

1 Introduction

Automotive electrification is expanding rapidly worldwide in response to the formidable challenges of greenhouse gas emissions and fossil oil depletion [1, 2]. Four-wheel-independent-drive electric vehicles (FWID EVs) have garnered attention in past years. They utilize four in-wheel motors (IWMs) to achieve direct propulsion [3], and the independent control of each wheel presents enormous potential for enhancing overall vehicle performance [4, 5]. In the meantime, vehicle safety control (VSC) systems, such as active suspension system (ASS) and anti-lock braking system (ABS), are being increasely used in production vehicle models [6]. The coordinated control of these systems holds promise for simultaneously enhancing vehicle handling performance and ride comfort during braking execution [7, 8].

In previous studies, ASS has been often employed to optimize vehicle ride comfort by directly controlling suspension actuation forces. It can also contributes to mitigating the negative impact of increased unsprung mass resulting from the use of in-wheel motors in FWID EVs. Numerous research endeavors have been dedicated to developing effective ASS controllers to optimize sprung mass acceleration based on quarter-vehicle dynamics modeling [9]. Commonly used control methods include explicit model predictive control (MPC) [10], fuzzy logic control [11], ceiling damping control [12], sliding mode control [13], H_∞ control [14] and others. In particular, H_∞

*Correspondence:
Lei Zhang
lei_zhang@bit.edu.cn
Shaohua Li
lshsjz@163.com
[1] National Engineering Research Center for Electric Vehicles, Beijing Institute of Technology, Beijing 100081, China
[2] State Key Laboratory of Mechanical Behavior and System Safety of Traffic Engineering Structures, Shijiazhuang Tiedao University, Shijiazhuang 050043, China

control is favored over other control algorithms due to its robustness to actuator faults, control network delays, and model uncertainties [15]. However, the conventional quarter-vehicle model cannot describe the pitch motion of vehicle. To address this limitation, researchers proposed half/full-vehicle models to account for vertical vibration and pitch motion of vehicle. For example, Sun et al. [16] presented an adaptive back-stepping ASS controller based on a half-vehicle model. Similarly, Youn et al. [17] proposed a linear quadratic optimal level-attitude ASS controller by employing a full-vehicle model. These studies to a large extent mitigated the pitch and level vibrations without considering load transfer during braking execution.

ABS implementation in FWID EVs can be realized either by conventional hydraulic braking or by regenerative braking [18]. Researchers have devoted significant efforts towards efficiently implementing ABS under varying driving conditions, using slide mode control, MPC, and H_2/H_∞ mixed control. Slide mode control is widely used to design wheel slip regulators and to develop nonlinear sliding observers for tire slip ratio and friction force estimation [18, 19]. To improve vehicle stability during braking execution, a sliding mode variable structure controller has been developed to regulate the wheel slip ratio near its optimal value [20]. Other approaches include MPC based on three-point road friction estimation [21] and H_2/H_∞ mixed control for slip ratio search optimization [22]. Generally, the primary control objective of these studies is to regulate the wheel slip ratio to track the reference or to keep it within a specified range. However, the existing methods have constantly overlooked the influence of tire vertical motion on the performance of ABS.

The implementation of ASS and ABS can result in coupled vertical and longitudinal vehicle dynamics. The integrated control of ASS and ABS has the potential to further enhance braking performance. In Ref. [23], Lin et al. simulated the implementations of ABS and ASS using a quarter-car model. They proposed a two-back-stepping controller to achieve independent control of these systems, and optimized the braking performance by controlling tire deflection and normal tire force. However, they failed to consider the impact of ASS control on vehicle vertical motion. Similarly, Lu et al. [24] introduced a fuzzy sliding mode control scheme that coordinates the control of a semi-active suspension system with a braking and steering control system. Nevertheless, there are few studies investigating the coupled effects of ASS and ABS on vehicle motions for FWID EVs [25]. Besides, the rapid changes in braking torque during ABS implementation can possibly induce severe pitch motions of the sprung mass and fluctuation of the load transfer, making it challenging for the controlled wheels to track the optimal slip ratio. Moreover, these pitching motions can significantly compromise vehicle ride comfort.

This study aims to address the aforementioned research gaps by developing an integrated control scheme for ASS and ABS to improve the ride comfort and handling performance of FWID EVs. To achieve this objective, a longitudinal-vertical coupled vehicle dynamics model is first established by integrating a road input model. Then the coupling mechanisms between the longitudinal and vertical vehicle dynamics are analyzed. An H_∞ controller for ASS control and a neural network sliding mode control (NNSMC) for ABS control are respectively proposed. Finally, the effectiveness of the integrated control scheme is verified through comprehensive hardware-in-loop (HIL) tests. The exclusive contributions of this study to the related research can be summarized as follows.

- A comprehensive full-vehicle longitudinal-vertical coupled dynamics model is developed by incorporating the dynamics of IWMs.
- The load transfer resulting from vehicle pitch motion during braking execution is considered as an external disturbance to ASS to improve the robustness of the proposed controller to vehicle longitudinal dynamics.
- An integrated ABS-ASS control scheme is proposed to improve braking safety while maintaining ride comfort, particularly in emergency braking scenarios.

The remainder of this paper is organized as follows: Section 2 introduces the longitudinal-vertical coupled vehicle dynamics model combined with the road input model. Section 3 discusses the interactions between ASS and ABS during the braking process, and provides a detailed description about the proposed integrated control scheme. Section 4 verifies the effectiveness of the proposed control scheme through HIL tests. Finally, the key conclusions drawn from this study are summarized in Section 5.

2 Longitudinal-Vertical Coupling Vehicle Dynamics Model

The coupling effect between longitudinal and vertical vehicle motions primarily arises from nonlinear dynamics of tire. Particularly during braking maneuvers, vehicle deceleration induces load transfer between the front and rear axles, influencing both the vertical motion of the vehicle and the interactions between tires and road. Hence, it becomes crucial to accurately model the longitudinal-vertical coupling relationship when implementing longitudinal and vertical vehicle control strategies during braking.

2.1 Full Vehicle Models

A comprehensive 7-Degree-of-Freedom (7-DOF) vehicle model is developed by incorporating the vertical translation and pitch motions of the sprung mass, horizontal translation of the vehicle, and vertical translation and rolling motions of the front and rear wheels, as illustrated in Figure 1.

In Figure 1, the suspension force F_i is the normal force generated by the load transfer with the subscripts *i=fl, fr, rl, rr* representing the left front, right front, left rear, and right rear wheels, respectively; m_{bi} is the equivalent quarter sprung mass; k_{si} and c_{si} are the suspension stiffness and damping coefficients, respectively; m_{si} is the stator and axle mass of IWM; m_{ri} is the equivalent overall mass of the IWM rotor and tire; k_b is the bearing stiffness of IWM; k_t is the tire stiffness; T_{bi} is the braking torque; F_{xi} is the frictional force transferred from road to tires; u_i is the active suspension actuation force; l_f, l_r, and h_g are the distances from the Centre-of-Cravity (CoG) of the sprung mass to the front axle, rear axle and road surface, respectively; x_s is the longitudinal displacement of the sprung mass; φ is the pitch angle of the vehicle body; ω_i is the angular speed of tires.

The dynamics of the sprung mass are given by [26]

$$\begin{aligned} m_s\ddot{z}_s &= F_{sfr} + F_{sfl} + F_{srr} + F_{srl}, \\ m_s\ddot{x}_s &= \sum F_{xi}, i = fl, fr, rl, rr, \\ I_s\ddot{\varphi} &= -l_f\left(F_{sfr} + F_{sfl}\right) + l_r(F_{srr} + F_{srl}) - m_s\ddot{x}_s h_g/g, \end{aligned} \tag{1}$$

where m_s is the sprung mass; z_s is the vertical displacement of the sprung mass; F_{si} is the vertical suspension force; I_s is the pitch rotational inertia of vehicle. F_{si} can be calculated by

$$\begin{aligned} F_{sfl} = F_{sfr} &= k_{sfl}(z_{sfl} - z_{bfl}) + c_{sfl}(\dot{z}_{sfl} - \dot{z}_{bfl}) + u_{fl}, \\ F_{srl} = F_{srr} &= k_{srl}(z_{srl} - z_{brl}) + c_{srl}(\dot{z}_{srl} - \dot{z}_{brl}) + u_{rl}. \end{aligned} \tag{2}$$

The center of the sprung mass moves forward during the braking process, and the normal force transmitted by the load transfer can be given by [27]

$$\begin{aligned} F_{fr} = F_{fl} &= -\ddot{x}_s m_s h_g/2g(l_r + l_f), \\ F_{rr} = F_{rl} &= \ddot{x}_s m_s h_g/2g(l_r + l_f). \end{aligned} \tag{3}$$

From Eq. (3), it can be seen that the longitudinal acceleration affects the vertical suspension force, which represents the coupling effect between the longitudinal and vertical motions.

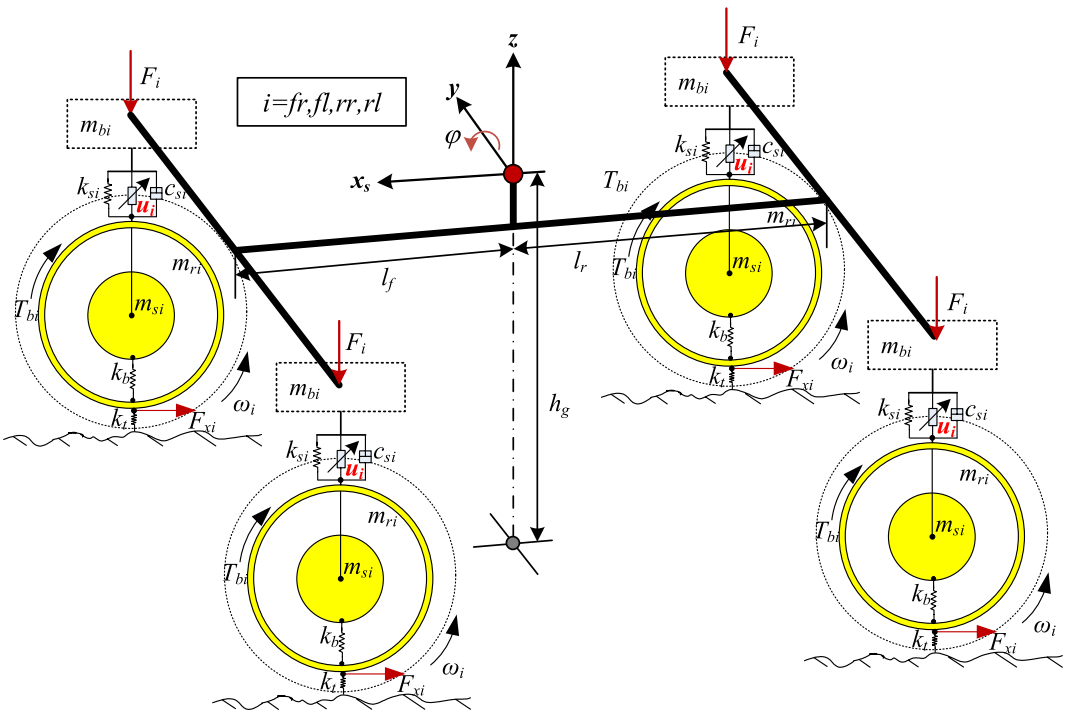

Figure 1 Vehicle dynamics model

Based on the Newton's law, the dynamic equation of the quarter vertical vibration model can be given by

$$\begin{cases} z_{bfl} = z_{bfr} = z_s - l_f \sin(\varphi), \\ z_{brl} = z_{brr} = z_s + l_r \sin(\varphi), \\ m_{bfl} = m_{bfr} = m_s l_r / 2(l_r + l_f), \\ m_{brl} = m_{brr} = m_s l_f / 2(l_r + l_f), \\ m_{si}\ddot{z}_{si} + F_{si} + k_b(z_{si} - z_{ri}) = 0, \\ m_{ri}\ddot{z}_{ri} + k_t(z_{ri} - q_i) + k_b(z_{ri} - z_{si}) = 0, \\ F_{zi} = m_{bi} + m_{si} + m_{ri} - k_t(z_{ri} - q_i), \\ i = fl, fr, rl, rr, \end{cases} \tag{4}$$

where z_{bi}, z_{si} and z_{ri} represent the vertical displacements of the equivalent quarter sprung mass, stator mass and rotor mass of IWM, with the subscript "i" representing the wheel position; F_{zi} is the vertical tire force; q_i is the generated road profile. The nonlinear magic formula (MF) model is employed to calculate the tire force due to its high fitting accuracy with test data [28]. A longitudinal single-wheel dynamics model can be given by

$$\begin{cases} F_{xi} = F_{zi}\mu(\lambda_i)\sin(C\arctan(B\lambda_i - E(B\lambda_i - \arctan(B\lambda_i)))), \\ I_i\dot{\omega}_i = T_{bi} - RF_{xi}, \\ i = fl, fr, rl, r, \end{cases} \tag{5}$$

where λ_i is the wheel slip ratio; μ is the tire-road adhesion coefficient; B, C, and E are the parameters of the MF model; I_i is the rotational inertia of each wheel; R is the effective wheel radius.

2.2 Road Input Model

The road grade (RG) and road type (RT) are considered in the road input model. RG represents the vertical road profiles for generating different vertical wheel movements, while RT characterizes the longitudinal road friction.

(1) Vertical road input

The power spectral density can describe the statistical characteristics of RG in the vertical direction. The Harmonic superposition algorithm is used to generate the time-domain road profiles as [29, 30]

$$q(t) = \sum_{k=1}^{M} \sqrt{2 \cdot G_q(f_{\text{mid}-k}) \cdot \frac{f_2 - f_1}{M}} \cdot \sin\left(2\pi f_{\text{mid}-k} + \chi_k\right), \tag{6}$$

where $f_{\text{mid-}k}$ is the kth middle frequency, k=1, 2, …, M; G_q ($f_{\text{mid-}K}$) is the power spectral density at $f_{\text{mid-}K}$; χ_k is an identifiably distributed phase with a range of [0, 2π]. The upper and lower time-domain frequency boundaries are denoted as f_1 and f_2, respectively. According to ISO-8608 [31], the road profiles of ISO-A, ISO-B and ISO-C are shown in Figure 2.

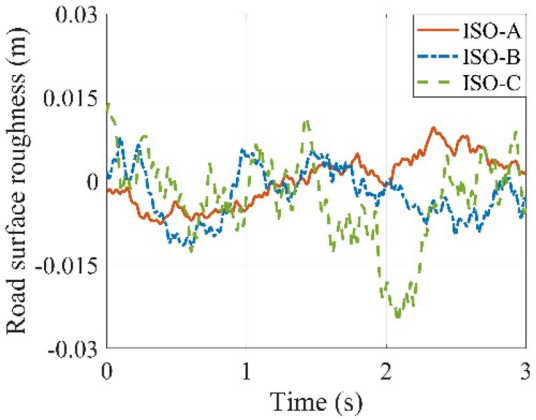

Figure 2 Road profiles of three typical roads

Table 1 Road condition constants

Road type	c_1	c_2	c_3	λ^*
Dry asphalt	1.28	23.99	0.52	0.17
Wet asphalt	0.86	33.82	0.35	0.12
Dry concrete	1.37	6.46	0.67	0.16
Cobble wet	0.40	33.71	0.12	0.12
Cobble dry	1.20	25.17	0.54	0.4
Snow	0.19	94.13	0.06	0.07
Ice	0.05	306.39	0	0.04

(2) Longitudinal road input

The longitudinal friction force is transferred to the vehicle through tire-road interactions. The tire-road adhesion coefficient μ and the reference slip ratio λ^* can be given by

$$\begin{cases} \mu(\lambda) = c_1\left(1 - e^{-c_2\lambda}\right) - c_3\lambda, \\ \lambda^* = \dfrac{1}{c_2}\text{In}\dfrac{c_1c_2}{c_3}, \end{cases} \tag{7}$$

where c_1, c_2, and c_3 define the road friction conditions (see Table 1) [27]. The rightmost column of Table 1 is the reference slip ratio λ^*, around which the peak adhesion coefficient can be obtained.

3 Design of the ASS and ABS Controllers

The ASS and ABS controllers are respectively developed in the integrated control framework base on the longitudinal-vertical coupling vehicle model.

3.1 Design of the ASS Controller

An ASS controller is developed to achieve the desirable suspension response in the stationary state, such as sprung mass motion, suspension deflection, and tire deflection [32]. A robust H_∞ control scheme is established to derive the external control forces for realizing desired vehicle states.

The vehicle is assumed to operate under pure braking conditions by ignoring vehicle yaw motion. Due to the symmetrical characteristics of the vehicle, the left half-vehicle model is selected as the control object. When φ is small with $\sin(\varphi)\approx\varphi$, the equivalent half-vehicle model can be expressed as

$$\begin{aligned}
\ddot{z}_{bfl} &= \ddot{z}_s - l_f\ddot{\varphi} = 2(F_{sfl}+F_{srl})/m_s \\
&\quad - l_f(-2l_fF_{sfl}+2l_rF_{srl}-m_s\ddot{x}_sh_g/g)/I_s, \\
\ddot{z}_{brl} &= \ddot{z}_s + l_r\ddot{\varphi} = 2(F_{sfl}+F_{srl})/m_s \\
&\quad + l_r(-2l_fF_{sfl}+2l_rF_{srl}-m_s\ddot{x}_sh_g/g)/I_s, \\
\ddot{z}_{sfl} &= -(F_{sfl}+k_b(z_{sfl}-z_{rfl}))/m_{sfl}, \\
\ddot{z}_{srl} &= -(F_{srl}+k_b(z_{srl}-z_{rrl}))/m_{srl}, \\
\ddot{z}_{rfl} &= -(k_t(z_{rfl}-q_{fl})+k_b(z_{rfl}-z_{sfl}))/m_{rfl}, \\
\ddot{z}_{rrl} &= -(k_t(z_{rrl}-q_{rl})+k_b(z_{rrl}-z_{srl}))/m_{rrl}.
\end{aligned} \tag{8}$$

The state vector is given by

$$\begin{aligned}
&\boldsymbol{x}(t) = \\
&[\dot{z}_{bfl}\ \dot{z}_{brl}\ \dot{z}_{sfl}\ \dot{z}_{srl}\ \dot{z}_{rfl}\ \dot{z}_{rrl}\ z_{bfl}-z_{sfl}\cdots \\
&z_{brl}-z_{srl}\ z_{sfl}-z_{rfl}\ z_{srl}-z_{rrl}\ z_{rfl}-q_{fl}\ z_{rrl}-q_{rl}]^{\mathrm{T}}.
\end{aligned} \tag{9}$$

The dynamic equations of the ASS system can be written as

$$\dot{\boldsymbol{x}}(t) = \boldsymbol{A}\boldsymbol{x}(t) + \boldsymbol{B}_w\boldsymbol{w}(t) + \boldsymbol{B}_u\boldsymbol{u}(t). \tag{10}$$

By substituting Eqs. (9) and (10) into Eq. (8), the state space can be rewritten as

$$\boldsymbol{B}_w = \begin{bmatrix} \frac{l_fm_sh_g}{gI_s} & \frac{-l_rm_sh_g}{gI_s} & \mathbf{0}_{1\times8} & 0 & 0 \\ 0 & 0 & \mathbf{0}_{1\times8} & -1 & 0 \\ 0 & 0 & \mathbf{0}_{1\times8} & 0 & -1 \end{bmatrix}^{\mathrm{T}},$$

$$\boldsymbol{w}(t) = \begin{bmatrix} \ddot{x}_s & \dot{q}_{fl} & \dot{q}_{rl} \end{bmatrix}^{\mathrm{T}},$$

$$\boldsymbol{B}_u = \begin{bmatrix} \frac{2}{m_s}+\frac{2l_f^2}{I_s} & \frac{2}{m_s}-\frac{2l_rl_f}{I_s} & -\frac{1}{m_{sfl}} & 0 & \mathbf{0}_{1\times8} \\ \frac{2}{m_s}-\frac{2l_rl_f}{I_s} & \frac{2}{m_s}+\frac{2l_r^2}{I_s} & 0 & -\frac{1}{m_{srl}} & \mathbf{0}_{1\times8} \end{bmatrix}^{\mathrm{T}},$$

$$\boldsymbol{u}(t) = \begin{bmatrix} u_{fl} & u_{rl} \end{bmatrix}^{\mathrm{T}}.$$

The ASS performance is typically assessed using the criteria such as ride comfort, suspension working space, and tire-road adhesion. Furthermore, the vertical-longitudinal coupling effect that occurs during braking leads to pitch movement of vehicle, resulting in load transfer and compromising vehicle stability. To evaluate system response, the acceleration of the sprung mass and the angular acceleration of the pitch motion are studied. The former is used to evaluate the ride comfort while the latter reflects the handling stability during braking.

In the meantime, it is essential to ensure that the suspension deflection and the air gap between the stator and rotor of IWM must maintain within a specified range to prevent structural failure. Furthermore, the output force of the ASS actuator is constrained due to limited power supply. Considering these conditions, the regulated output $\boldsymbol{z}_1$ and the normalized constraint output $\boldsymbol{z}_2$ are defined as

$$\boldsymbol{A} = \begin{bmatrix}
-\frac{2c_{sfl}}{m_s} & -\frac{2c_{sfl}l_f^2}{I_s} & -\frac{2c_{srl}}{m_s}+\frac{2c_{srl}l_fl_r}{I_s} & \frac{2c_{sfl}}{m_s}+\frac{2c_{sfl}l_f^2}{I_s} & \frac{2c_{srl}}{m_s}-\frac{2c_{srl}l_fl_r}{I_s} & 0 & 0 & -\frac{2k_{sfl}}{m_s} & -\frac{2k_{sfl}l_f^2}{I_s} & -\frac{2k_{srl}}{m_s}+\frac{2k_{srl}l_fl_r}{I_s} & 0 & 0 & 0 & 0 \\
-\frac{2c_{sfl}}{m_s}+\frac{2c_{sfl}l_rl_f}{I_s} & -\frac{2c_{srl}}{m_s}-\frac{2c_{srl}l_r^2}{I_s} & \frac{2c_{sfl}}{m_s}-\frac{2c_{sfl}l_rl_f}{I_s} & \frac{2c_{srl}}{m_s}+\frac{2c_{srl}l_r^2}{I_s} & 0 & 0 & -\frac{2k_{sfl}}{m_s}+\frac{2k_{sfl}l_rl_f}{I_s} & -\frac{2k_{srl}}{m_s}-\frac{2k_{srl}l_r^2}{I_s} & 0 & 0 & 0 & 0 & 0 \\
\frac{c_{sfl}}{m_{sfl}} & 0 & -\frac{c_{sfl}}{m_{sfl}} & 0 & 0 & 0 & \frac{k_{sfl}}{m_{sfl}} & 0 & -\frac{k_b}{m_{sfl}} & 0 & 0 & 0 & 0 \\
0 & \frac{c_{srl}}{m_{srl}} & 0 & -\frac{c_{srl}}{m_{srl}} & 0 & 0 & 0 & \frac{k_{srl}}{m_{srl}} & 0 & -\frac{k_b}{m_{srl}} & 0 & 0 & 0 \\
0 & 0 & 0 & 0 & 0 & 0 & 0 & 0 & \frac{k_b}{m_{rfl}} & 0 & -\frac{k_t}{m_{rfl}} & 0 & 0 \\
0 & 0 & 0 & 0 & 0 & 0 & 0 & 0 & 0 & \frac{k_b}{m_{rrl}} & 0 & -\frac{k_t}{m_{rrl}} & 0 \\
1 & 0 & -1 & 0 & 0 & 0 & 0 & 0 & 0 & 0 & 0 & 0 & 0 \\
0 & 1 & 0 & -1 & 0 & 0 & 0 & 0 & 0 & 0 & 0 & 0 & 0 \\
0 & 0 & 1 & 0 & -1 & 0 & 0 & 0 & 0 & 0 & 0 & 0 & 0 \\
0 & 0 & 0 & 1 & 0 & -1 & 0 & 0 & 0 & 0 & 0 & 0 & 0 \\
0 & 0 & 0 & 0 & 1 & 0 & 0 & 0 & 0 & 0 & 0 & 0 & 0 \\
0 & 0 & 0 & 0 & 0 & 1 & 0 & 0 & 0 & 0 & 0 & 0 & 0
\end{bmatrix},$$

$$\begin{aligned}\boldsymbol{z}_1 &= [\,\ddot{z}_s \;\; \ddot{\varphi}\,]^{\mathrm{T}} \\ &= \boldsymbol{C}_{x1}\boldsymbol{x}(t) + \boldsymbol{D}_{w1}\boldsymbol{w}(t) + \boldsymbol{D}_{u1}\boldsymbol{u}(t), \\ \boldsymbol{z}_2 &= \left[\frac{z_{bfl}-z_{sfl}}{z_{flm}} \quad \frac{z_{brl}-z_{srl}}{z_{rlm}} \quad \frac{z_{rfl}-z_{sfl}}{z_{flam}} \cdots \right. \\ &\quad \left. \frac{z_{rrl}-z_{srl}}{z_{rlam}} \quad \frac{u_{fl}}{u_{flm}} \quad \frac{u_{fr}}{u_{rlm}}\right]^{\mathrm{T}} \\ &= \boldsymbol{C}_{x2}\boldsymbol{x}(t) + \boldsymbol{D}_{u2}\boldsymbol{u}(t),\end{aligned} \tag{11}$$

where

$$\boldsymbol{C}_{x1} = \begin{bmatrix} \frac{-2c_{sfl}}{m_s} & \frac{-2c_{srl}}{m_s} & \frac{2c_{sfl}}{m_s} & \frac{2c_{srl}}{m_s} & \boldsymbol{0}_{1\times2} & \frac{-2k_{sfl}}{m_s} & \frac{-2k_{srl}}{m_s} & \boldsymbol{0}_{1\times4} \\ \frac{2l_f c_{sfl}}{I_s} & \frac{-2l_r c_{srl}}{I_s} & \frac{-2l_f c_{sfl}}{I_s} & \frac{2l_r c_{srl}}{I_s} & \boldsymbol{0}_{1\times2} & \frac{2l_f k_{sfl}}{I_s} & \frac{-2l_r k_{srl}}{I_s} & \boldsymbol{0}_{1\times4} \end{bmatrix},$$

$$\boldsymbol{D}_{w1} = \begin{bmatrix} 0 & 0 & 0 \\ \frac{-m_s h_g}{gI_s} & 0 & 0 \end{bmatrix}, \boldsymbol{D}_{u1} = \begin{bmatrix} \frac{2}{m_s} & \frac{2}{m_s} \\ \frac{-2l_f}{I_s} & \frac{2l_r}{I_s} \end{bmatrix},$$

$$\boldsymbol{C}_{x2} = \begin{bmatrix} \boldsymbol{0}_{1\times6} & z_{flm}^{-1} & 0 & 0 & 0 & \boldsymbol{0}_{1\times2} \\ \boldsymbol{0}_{1\times6} & 0 & z_{rlm}^{-1} & 0 & 0 & \boldsymbol{0}_{1\times2} \\ \boldsymbol{0}_{1\times6} & 0 & 0 & z_{flam}^{-1} & 0 & \boldsymbol{0}_{1\times2} \\ \boldsymbol{0}_{1\times6} & 0 & 0 & 0 & z_{rlam}^{-1} & \boldsymbol{0}_{1\times2} \\ \boldsymbol{0}_{1\times6} & 0 & 0 & 0 & 0 & \boldsymbol{0}_{1\times2} \\ \boldsymbol{0}_{1\times6} & 0 & 0 & 0 & 0 & \boldsymbol{0}_{1\times2} \end{bmatrix},$$

$$\boldsymbol{D}_{u2} = \begin{bmatrix} \boldsymbol{0}_{1\times4} & u_{flm}^{-1} & 0 \\ \boldsymbol{0}_{1\times4} & 0 & u_{rlm}^{-1} \end{bmatrix}^{\mathrm{T}}$$

, z_{ilm} is the maximum suspension deflection; z_{ilam} is the maximum air gap of IWM; u_{ilm} is the maximum output force of the actuator. The subscript, *i*=*f*, *r*, represent the front and rear wheels, respectively.

The designed state feedback controller $\boldsymbol{u}(t) = \boldsymbol{K}\boldsymbol{x}(t)$ holds under the following assumptions.

(1) Without external perturbations, the closed-loop system described in Eqs. (10) and (11) is asymptotically stable.
(2) The performance $\|\boldsymbol{z}_1(t)\|_\infty \le \gamma\|w(t)\|_\infty$ is minimized subject to Eqs. (10) and (11), where γ is the anti-disturbance level of the H_∞ controller.
(3) The time-domain constraint $|\boldsymbol{z}_2(t)| \le 1|\boldsymbol{z}_2(t)|\le1$ must be satisfied.

The parameters of the robust H_∞ controller can be obtained by solving the following theorem.

Theorem

If there exist positive scalars ρ and γ and a positive definite symmetric matrix $\boldsymbol{X}$ that make the inequalities described in Eqs. (12) and (13) hold at any time instant under LMIs, the system is globally asymptotic stable. In Eq. (13), ρ^2=$w_{\max}\gamma^2$, and $w_{\max}$ is the upper perturbation energy of $\boldsymbol{w}(t)$. $\boldsymbol{K}$=$\boldsymbol{W}\boldsymbol{X}^{-1}$ can be used to derive the state feedback gain $\boldsymbol{K}$, and the detailed proof is given in Ref. [33],

$$\begin{bmatrix} (\boldsymbol{A}\boldsymbol{X}+\boldsymbol{B}_u\boldsymbol{W})^{\mathrm{T}} + (\boldsymbol{A}\boldsymbol{X}+\boldsymbol{B}_u\boldsymbol{W}) & \boldsymbol{B}_w & (\boldsymbol{C}_{x1}\boldsymbol{X}+\boldsymbol{D}_{u1}\boldsymbol{W})^{\mathrm{T}} \\ \boldsymbol{B}_w^{\mathrm{T}} & -\gamma^2\boldsymbol{I} & \boldsymbol{D}_{w1}^{\mathrm{T}} \\ \boldsymbol{C}_{x1}\boldsymbol{X}+\boldsymbol{D}_{u1}\boldsymbol{W} & \boldsymbol{D}_{w1} & -\boldsymbol{I} \end{bmatrix} < 0, \tag{12}$$

$$\begin{bmatrix} -\boldsymbol{X} & \boldsymbol{C}_{x2}\boldsymbol{X}+\boldsymbol{D}_{u2}\boldsymbol{W} \\ (\boldsymbol{C}_{x2}\boldsymbol{X}+\boldsymbol{D}_{u2}\boldsymbol{W})^{\mathrm{T}} & -\frac{1}{\rho}\boldsymbol{I} \end{bmatrix} < 0. \tag{13}$$

3.2 Design of the ABS Controller

The neural network sliding mode control (NNSMC) has gained widespread recognition due to its capability to accommodate system constraints in many applications [34, 35]. In this study, NNSMC is employed to track the optimal slip ratio λ^* during the braking process. The wheel slip ratio is defined as

$$\lambda_i = \frac{v_s - \omega_i R}{v_s}, \tag{14}$$

where v_s is the longitudinal vehicle velocity.

Define the sliding surface as

$$\begin{aligned} s &= e = \lambda^* - \lambda_i, \\ \dot{s} &= -\dot{\lambda}_i. \end{aligned} \tag{15}$$

The differentiation of Eq. (14) is obtained as

$$\begin{aligned}\dot{\lambda}_i &= \left(1 - \frac{\omega_i R}{v_s}\right)' = -\left(\frac{\dot{\omega}_i R}{v_s} - \frac{\dot{v}_s \omega_i R}{v_s^2}\right) \\ &= \frac{\dot{v}_s\omega_i R - v_s\dot{\omega}_i R}{\dot{v}_s^2}.\end{aligned} \tag{16}$$

The single-wheel dynamics model can be given by

$$\dot{\omega}_i = \frac{T_b}{I_i} - \frac{RF_{xi}}{I_i}. \tag{17}$$

By substituting Eq. (17) into Eq. (16), we get

$$\begin{aligned}\dot{\lambda}_i &= \frac{\dot{v}_s\omega_i R}{v_s^2} + \frac{R^2}{v_s I_s}F_{xi} - \frac{T_{bi}R}{v_s I_s} + d \\ &= GF_{xi} + PT_{bi} + D + d,\end{aligned} \tag{18}$$

where $G = \frac{\omega_i R}{m_s v_s^2}$, $P = -\frac{R}{v_s I_s}$, $D = \frac{\dot{v}_s R}{v_s^2}$, and d is the disturbance.

By substituting Eq. (18) into Eq. (15), we get

$$T_{bi} = -\frac{G}{P}\hat{F}_{xi} + \frac{\eta\,\mathrm{sign}(s) + D}{P}, \tag{19}$$

where $\hat{F}_{xi}$ is the estimated F_{xi}; η is the coefficient of the NNSMC controller.

The Lyapunov asymptotical stability condition can be rewritten as

$$\begin{aligned}\dot{L} &= s\cdot\dot{s}+\tau\tilde{\omega}_i^{\mathrm{T}}\dot{\tilde{\omega}}_i\\ &= s\left[-G\tilde{\omega}^{\mathrm{T}}h(x)-G\varepsilon-D-d-\eta\mathrm{sign}(s)\right]-\tau\tilde{\omega}^{\mathrm{T}}\dot{\hat{\omega}}\\ &= -\tilde{\omega}^{\mathrm{T}}\left[sGh(x)+\tau\dot{\hat{w}}\right]-s[G\varepsilon+D+d+\eta\mathrm{sign}(s)],\end{aligned} \tag{20}$$

where $\dot{\hat{\omega}}=-\frac{G}{\tau}s\cdot h(x)$, and τ and ε are the estimated error and the reaching law.

Let $|\eta|\geq\left|G\varepsilon+D+d\right|$, so that $\dot{L}<0$. The stability of the ABS controller is proven.

The PID controller is selected as a comparison to highlight the efficacy of the proposed contrller, which is given by

$$T_{bi}=K_P(\lambda-\lambda^*)+K_I\int_0^t(\lambda-\lambda^*)\mathrm{d}t+K_D\frac{\mathrm{d}(\lambda-\lambda^*)}{\mathrm{d}t}, \tag{21}$$

where K_P, K_I and K_D are the adjustable parameters of the PID controller.

Figure 3 presents a control block diagram illustrating the flowchart of the proposed integrated control scheme. To trigger ABS and ASS control, a hard brake maneuver is performed by the test vehicle on a straight road. In the developed longitudinal-vertical coupling model, the vertical tire motion is influenced by RG, while the longitudinal tire motion is affected by RT. During the braking process, the coupling effect between vertical and longitudinal vehicle dynamics primarily manifests in the sprung and unsprung masses. In the case of the sprung mass, the braking-induced load transfer induces pitching movement that impacts vehicle ride comfort. As for the unsprung mass, the coupling effect mainly occurs in the tires, where the vertical dynamic load significantly influences the longitudinal friction. The proposed integrated control scheme has a specific workflow, which is explained as follows: The ASS controller utilizes the vibration responses of components as inputs and generates an output force based on the synthesized control law. This ASS actuator output force effectively mitigates the load transfer caused by rapidly changing braking forces when ABS is activated, ensuring that the ABS controller can promptly track the peak tire-road adhesion and thus reduce the braking distance.

4 Hardware-in-Loop (HIL) Verifications

To thoroughly evaluate the effectiveness of the proposed control scheme, comprehensive Hardware-in-Loop (HIL) tests were conducted based on a dedicated HIL platform. Virtual real-time vehicle models were employed in combination with a real electronic control unit (ECU) to assess the performance and reliability of the developed control

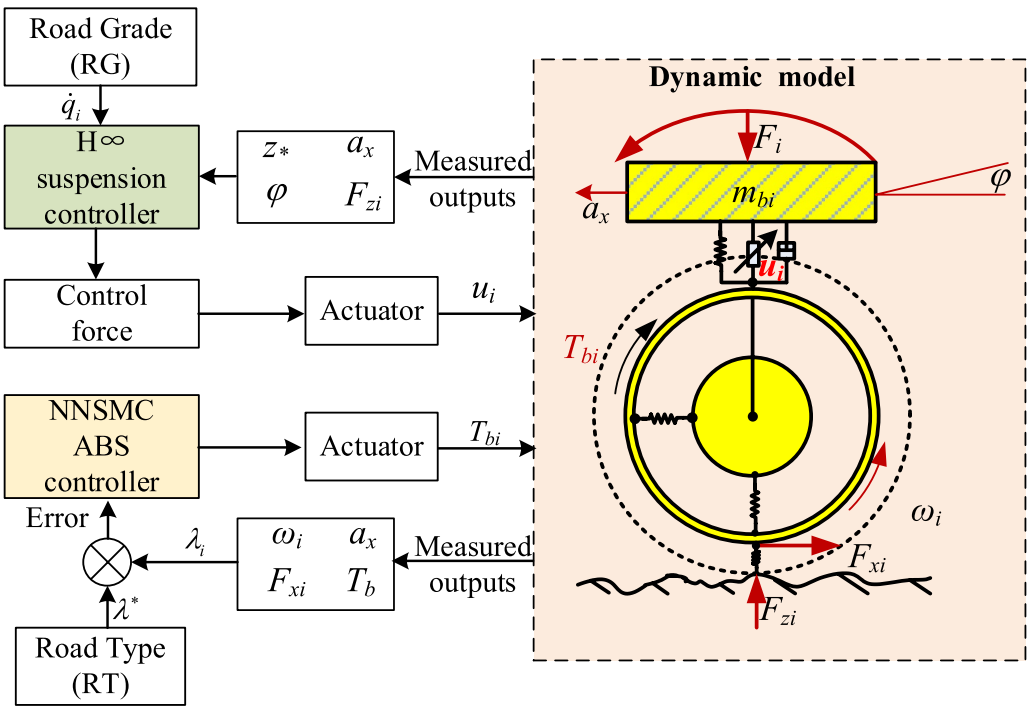

Figure 3 Schematic of the proposed integrated control scheme

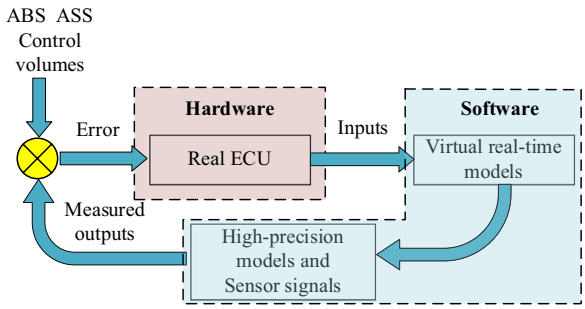

Figure 4 Block diagram of the HIL tests

strategy. Figure 4 illustrates the configuration and testing principle of the HIL platform.

Figure 5 depicts the HIL setup, which consists of two host computers, a real-time personal controller (RTPC), an OpenECU controller, a CANape, and a DC power source. LABCAR serves as a real-time vehicle simulator to provide a virtual environment for examing the efficacy of the control scheme. The resource configuration of LABCAR is performed using the LABCAR IP software on the host computer PC1, and the generated C code is downloaded to RTPC, operating with a cycle time of less than 0.1 ms. The ABS and ASS controllers in MATLAB/Simulink calculate the braking torque and the suspension force. The MATLAB/Simulink code is then compiled into executable codes and downloaded to the OpenECU controller for real-time implementation. The OpenECU controller is connected to LABCAR via the CAN bus, and CANape is utilized for signal collection and calibration.

The vehicle specifications are listed in Table 2, and the magnetic ride control active suspension is used as the actuator [36].

The ISO-B and dry asphalt roads are used in the HIL test. Prior to the execution of braking, the initial vehicle speed is set as 60 km/h. ABS deactivation occurs when the vehicle speed drops below 5 km/h. The LMI toolbox utilizes the solver-MINCX to determine the ASS actuation force. Through the LMI algorithm, the control gain matrix $\boldsymbol{K}$ for the active suspension controller is obtained, ensuring a guaranteed H_∞ performance index of γ=78 and ρ=0.17, which is given by

$$\boldsymbol{K} = \begin{bmatrix} 272 & 182 & 1789 & 2819 & 2649 & 2639... \\ 4714 & 1154 & 3.96\times10^5 & 2.53\times10^5 & 3.49\times10^5 & 2.05\times10^{-4}; \\ 318 & 238 & 1174 & 1745 & 1494 & 1505... \\ 2454 & 4822 & 8.23\times10^5 & 3.28\times10^5 & 3.78\times10^5 & 2.45\times10^{-4} \end{bmatrix}.$$

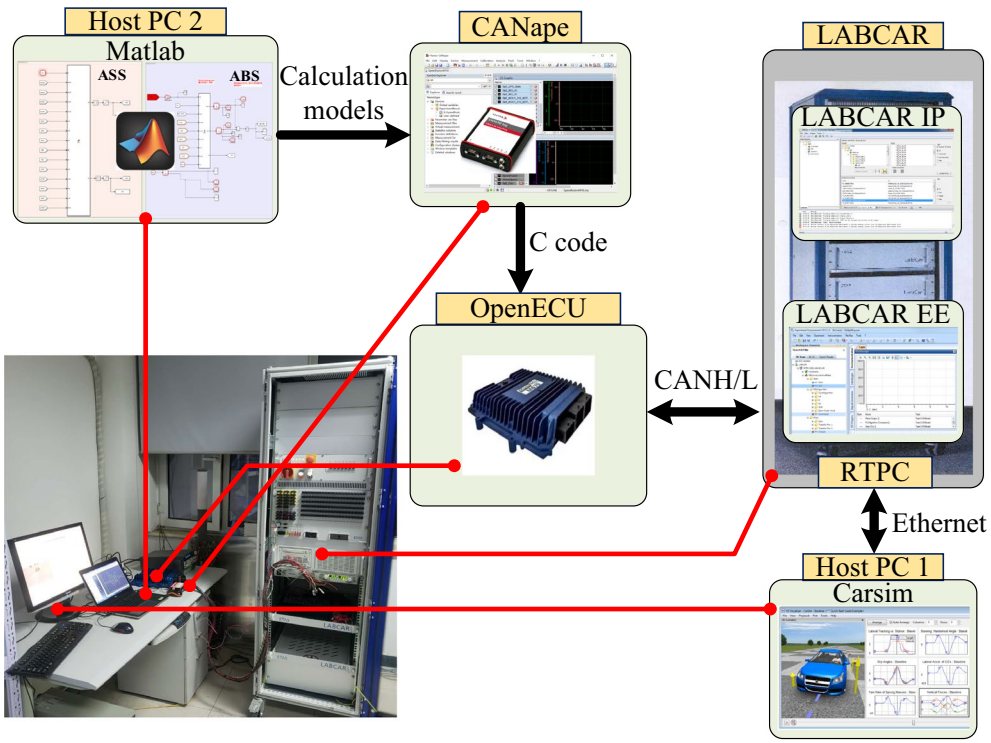

Figure 5 The HIL setup

Table 2 Specifications of the test vehicle

Parameters	Value
$k_{sfl} = k_{sfr}$ (N/m)	2.4×10^4
$k_{srl} = k_{srr}$ (N/m)	1.8×10^4
c_{si} (N·s/m)	1.8×10^3
k_b (N/m)	7×10^6
k_t (N/m)	2.2×10^5
c_t (N·s/m)	510
I_i (kg·m^2)	0.963
m_s (kg)	1328
m_{si} (kg)	34.5
m_{ri} (kg)	28.65
l_f (m)	0.993
l_r (m)	0.877
I_s (kg·m^2)	1926
h_g (m)	0.478
B	20.2937
C	1.9655
E	0.8613
Parameters of the designed controller	
$z_{flm} = z_{rlm}$ (m)	0.8
$z_{flam} = z_{rlam}$ (mm)	0.8
$u_{flm} = u_{rlm}$ (N)	2000

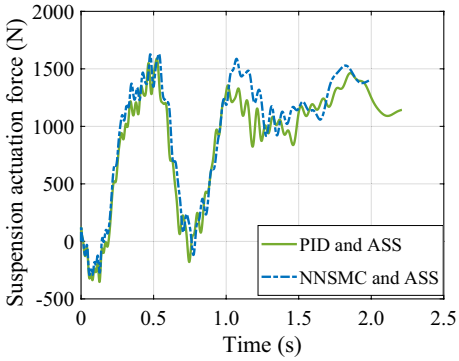

Figure 6 Actuation forces of the active suspension

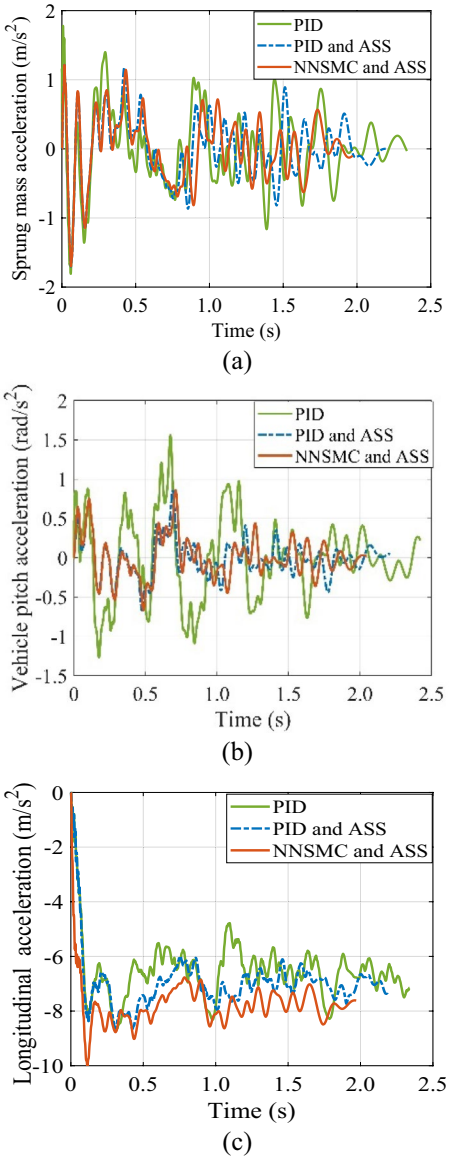

Figure 7 Comparison of vehicle acceleration response: (**a**) Acceleration of the sprung mass, (**b**) Pitch acceleration of the vehicle body, (**c**) Longitudinal acceleration of the sprung mass

Figure 6 illustrates the active suspension actuation forces under two scenarios. In both cases, the actuation forces remain below the threshold of u_{flm}. Additionally, the control force applied under the PID and ASS scheme is lower compared to the integrated NNSMC and ASS scheme, indicating that the latter necessitates higher force to counteract the adverse impact of braking on vertical vehicle motion.

The results of the HIL tests depicting the dynamic response of the sprung mass under road excitation are presented in Figure 7.

Figure 7 shows that the integrated NNSMC and ASS control scheme results in reduced vertical and pitch accelerations compared to the stand-alone PID and the PID with ASS controller. This indicates that the proposed control scheme surpasses traditional PID control in terms of ride comfort and handling stability. Notably, the sprung acceleration under road excitation is considerably optimized, indicating improved vehicle ride comfort, while the braking performance benefits from smoother

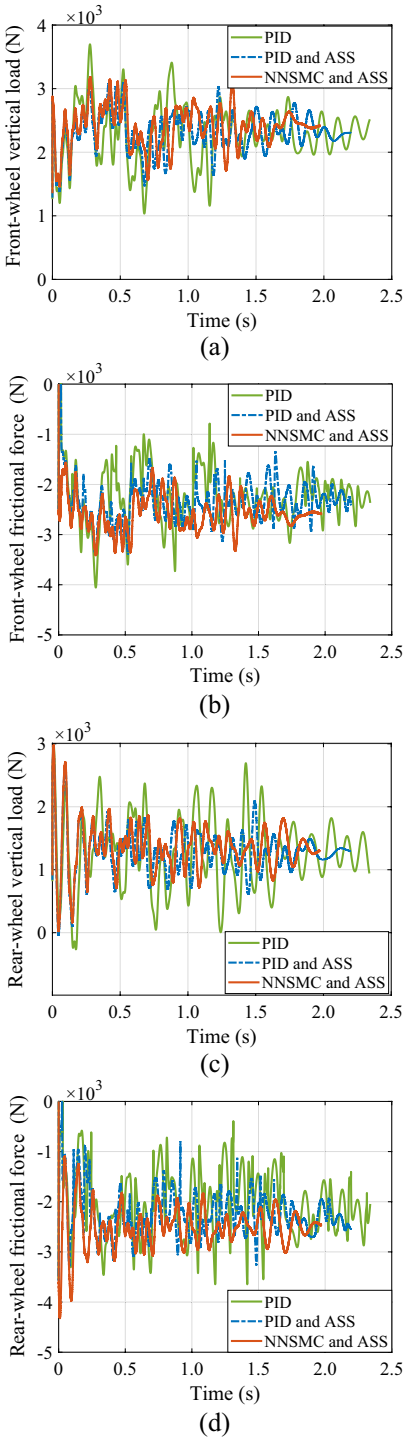

Figure 8 Comparison of the dynamic wheel loads and wheel slip ratios: (**a**) Front wheel vertical load, (**b**) Front-wheel frictional force, (**c**) Rear wheel vertical load, (**d**) Rear-wheel frictional force

vertical vehicle body movement. Additionally, the integrated control scheme demonstrates reduction in both the braking distance and the braking time.

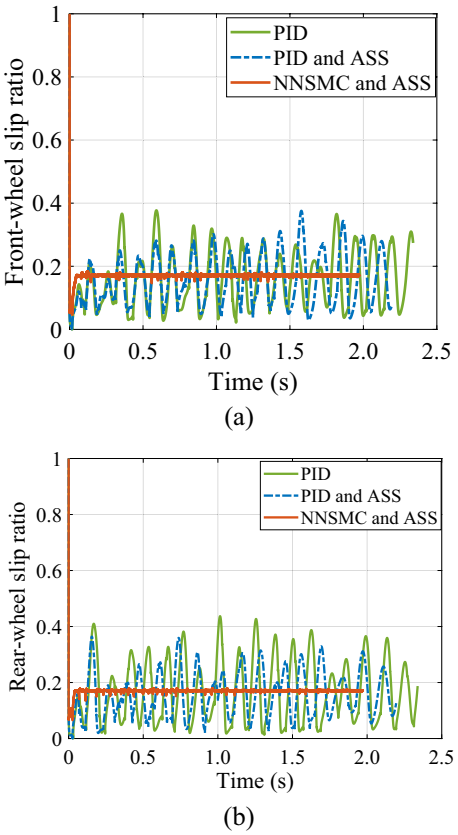

Figure 9 Comparison of the wheel slip ratios: (**a**) Front wheel slip ratio, (**b**) Rear wheel slip ratio

The dynamics of the wheel under different control strategies are illustrated in Figure 8.

Figures 8(a), (c) demonstrate the effective suppression of vertical load fluctuations on the front and rear wheels through the implementation of the NNSMC and ASS controller. This can be attributed to the active regulation of the vehicle body's pitching motion and the elimination of load transfer achieved by the proposed ASS controller. In Figures 8(b), (d), the introduction of ASS, in comparison to the PID controller, leads to reduced fluctuation in the longitudinal frictional force. Moreover, the integrated NNSMC and ASS exhibit more effective control of the frictional force compared to the combination of PID and ASS controllers, resulting in further suppression of the fluctuation of the longitudinal frictional force.

Figure 9 presents a comprehensive comparison of the ABS control target, i. e., the slip ratio.

Figures 9(a), (b) demonstrate the effectiveness of the integrated ABS and ASS control scheme through the HIL test on a single road surface. The smooth vertical load facilitates faster and smoother tracking of the optimal slip ratio by the ABS controller. The slip ratio remains stable around the optimal value. Furthermore, the proposed

Table 3 Statistical results between the comparison and proposed controller

Controller	RMS of $\ddot{z}_s$ (m/s^2)	Slip ratio SNR	t_s (s)	d_s (m)
PID	0.536	66.78%	2.42	22.8
PID and ASS	0.457–↓14.7%	49.88%	2.21–↓8.7%	21.2–↓7.1%
NNSMC and ASS	0.448– ↓16.4%	6.82%	2.05–↓15.3%	19.4– ↓14.9%

NNSMC control strategy for ABS outperforms the PID control in terms of optimal slip ratio tracking accuracy.

To further assess the effectiveness of the proposed integrated control scheme, statistical comparison results are presented in Table 3. The parameters evaluated include braking time (t_s) and braking distance (d_s). In order to accurately measure the error in slip ratio, the signal-to-noise ratio (SNR) is introduced as an evaluation metric. The slip ratio of the front wheel is considered as the target, which is given by

$$\mathrm{SNR} = \frac{\sqrt{\frac{1}{t}\int_0^t \left(\lambda_{fl}(t) - \lambda^*\right)^2 \mathrm{d}t}}{\lambda^*}. \tag{22}$$

Additionally, the root mean square error (RMS) is utilized to quantify the optimization effect. For a sequence that contains n elements, the RMS value-x_{rms} is given by

$$x_{rms} = \frac{\|x\|}{\sqrt{n}} = \sqrt{\frac{1}{n}\sum_{j=1}^{n} x_j^2}, \quad j = 1, \ldots, n. \tag{23}$$

In Table 3, it can be seen that the proposed integrated controller leads to an improvement of 16.4% in $\ddot{z}_s$. Additionally, the braking duration and distance are reduced by 15.3% and 14.9%, respectively. The evaluation indexes for both vertical and longitudinal performance surpass those of the integrated PID and ASS controller. In summary, the proposed integrated ASS and ABS controllers enhance vehicle braking performance while ensuring ride comfort.

5 Conclusions

This paper presents an integrated active suspension system (ASS) and anti-lock braking system (ABS) control scheme for four-wheel-independent-drive electric vehicles. To capture the longitudinal and vertical coupling effect of the vehicle, a comprehensive longitudinal-vertical coupled vehicle dynamics model is established by integrating a road input model. Furthermore, an H_∞ controller is designed for ASS, while a neural network sliding mode control (NNSMC) is developed for ABS. The effectiveness of the proposed scheme is thoroughly examined using a Hardware-in-Loop (HIL) platform. The results of the HIL tests demonstrate significant improvements achieved by the proposed control scheme. Specifically, the acceleration of the sprung mass and the pitch acceleration of the vehicle body are effectively reduced, leading to enhanced vehicle ride comfort. Moreover, the braking time and distance are reduced by 15.3% and 14.9%, respectively. These findings validate the efficacy of the proposed integrated control scheme in optimizing both braking performance and vehicle ride comfort.

Acknowledgements
Not applicable

Authors' Contributions
ZZ and LZ were in charge of the whole trial; XD wrote the manuscript; ZQZ, SL and LG assisted with sampling and laboratory analyses. All authors read and approved the final manuscript.

Funding
Supported by National Natural Science Foundation of China (Grant No. 52272387), State Key Laboratory of Mechanical Behavior and System Safety of Traffic Engineering Structures, Shijiazhuang Tiedao University of China (Grant No. KF2020-29), Beijing Municipal Science and Technology Commission through Beijing Nova Program of China (Grant No. 20230484475).

Availability of Data and Materials
The datasets supporting the conclusions of this article are included within the article.

Declarations

Ethics Approval and Consent to Participate
Not applicable.

Consent to Participate
Not applicable.

Competing Interests
The authors declare no competing financial interests.

Received: 7 December 2022 Revised: 4 January 2024 Accepted: 12 January 2024
Published online: 04 March 2024

References

[1] C Wang, Z Wang, L Zhang, et al. Post-impact motion planning and tracking control for autonomous vehicles. *Chinese Journal of Mechanical Engineering*, 2022, 35(1): 1–18.
[2] F Sun. Green energy and intelligent transportation—Promoting green and intelligent mobility. *Green Energy and Intelligent Transportation*, 2022, 100017.

[3] Z Zhao, H Taghavifar, H Du, et al. In-wheel motor vibration control for distributed-driven electric vehicles: A review. *IEEE Transactions on Transportation Electrification*, 2021, 7(4): 2864–2880.
[4] L Zhang, Z Zhang, Z Wang, et al. Chassis coordinated control for full x-by-wire vehicles-a review. *Chinese Journal of Mechanical Engineering*, 2021, 34(1): 1–25.
[5] Y Tong, C Li, G Wang, et al. Integrated path-following and fault-tolerant control for four-wheel independent-driving electric vehicles. *Automotive Innovation*, 2022, 5: 311–323
[6] H Zhang, C Liu, W Zhao. Segmented trajectory planning strategy for active collision avoidance system. *Green Energy and Intelligent Transportation*, 2022, 1(1): 100002.
[7] J Wang, S Gao, Y Qiang, et al. Structural topology and dynamic response analysis of an electric torque vectoring drive-axle for electric vehicles. *Automotive Innovation*, 2022, 5: 164–179.
[8] X Ding, Z Wang, L Zhang, et al. A comprehensive vehicle stability assessment system based on enabling tire force estimation. *IEEE Transactions on Vehicular Technology*, 2022, 71(11): 11571–11588.
[9] M M Fateh, S S Alavi. Impedance control of an active suspension system. *Mechatronics*, 2009, 19(1): 134–140.
[10] L H Csekő, M. Kvasnica, B Lantos. Explicit MPC-based RBF neural network controller design with discrete-time actual Kalman filter for semiactive suspension. *IEEE Transactions on Control Systems Technology*, 2015, 23(5): 1736–1753.
[11] M Shieh, J Chiou, M Liu. Design of immune-algorithm-based adaptive fuzzy controllers for active suspension systems. *Advances in Mechanical Engineering*, 2014, 6: 916257.
[12] M Sunwoo, K C Cheok, N Huang. Model reference adaptive control for vehicle active suspension systems. *IEEE Transactions on industrial electronics*, 1991, 38(3): 217–222.
[13] S Chen, J Wang, M Yao, et al. Improved optimal sliding mode control for a non-linear vehicle active suspension system. *Journal of Sound and Vibration*, 2017, 395: 1–25.
[14] P Badri, A Amini, M Sojoodi. Robust fixed-order dynamic output feedback controller design for nonlinear uncertain suspension system. *Mechanical Systems and Signal Processing*, 2016, 80: 137–151.
[15] J Marzbanrad, N Zahabi. H_∞ active control of a vehicle suspension system exited by harmonic and random roads. *Mechanics and Mechanical Engineering*, 2017, 21(1).
[16] W Sun, H Pan, H Gao. Filter-based adaptive vibration control for active vehicle suspensions with electrohydraulic actuators. *IEEE Transactions on Vehicular Technology*, 2015, 65(6): 4619–4626.
[17] I Youn, J Im, M Tomizuka. Level and attitude control of the active suspension system with integral and derivative action. *Vehicle System Dynamics*, 2006, 44(9): 659–674.
[18] Z Wang, Y Wang, L Zhang, et al. Vehicle stability enhancement through hierarchical control for a four-wheel-independently-actuated electric vehicle. *Energies*, 2017, 10(7): 947.
[19] L Li, X Li, X Wang, et al. Transient switching control strategy from regenerative braking to anti-lock braking with a semi-brake-by-wire system. *Vehicle System Dynamics*, 2016, 54(2): 231–257.
[20] K Han, B Lee, S B Choi. Development of an antilock brake system for electric vehicles without wheel slip and road friction information. *IEEE Transactions on Vehicular Technology*, 2019, 68(6): 5506–5517.
[21] B Wang, X Huang, J Wang, et al. A robust wheel slip ratio control design combining hydraulic and regenerative braking systems for in-wheel-motors-driven electric vehicles. *Journal of the Franklin Institute*, 2015, 352(2): 577–602.
[22] W Zhao, X Qin. Study on mixed H_2/H_∞ robust control strategy of four wheel steering system. *Science China Technological Sciences*, 2017, 60(12): 1831–1840.
[23] J Lin, W Ting. Nonlinear control design of anti-lock braking systems with assistance of active suspension. *IET control theory & applications*, 2007, 1(1): 343–348.
[24] S B Lu, Y N Li, S B Choi, et al. Integrated control on MR vehicle suspension system associated with braking and steering control. *Vehicle System Dynamics*, 2011, 49(1–2): 361–380.
[25] J Zhang, Y Yang, M Hu, et al. Longitudinal–vertical comprehensive control for four-wheel drive pure electric vehicle considering energy recovery and ride comfort. *Energy*, 2021, 236: 121417.
[26] S Hegazy, H Rahnejat, K Hussain. Multi-body dynamics in full-vehicle handling analysis under transient manoeuvre. *Vehicle System Dynamics*, 2000, 34(1): 1–24.
[27] R Rajamani. Vehicle dynamics and control. *Springer Science & Business Media*, 2011.
[28] I Besselink, A Schmeitz, H Pacejka. An improved magic formula/swift tyre model that can handle inflation pressure changes. *Vehicle System Dynamics*, 2010, 48(S1): 337–352.
[29] Y Qin, Z Wang, C Xiang, et al. Speed independent road classification strategy based on vehicle response: Theory and experimental validation. *Mechanical Systems and Signal Processing*, 2019, 117: 653–666.
[30] Y Qin, C Wei, X Tang, et al. A novel nonlinear road profile classification approach for controllable suspension system: Simulation and experimental validation. *Mechanical Systems and Signal Processing*, 2019, 125: 79–98.
[31] P Múčka. Simulated road profiles according to ISO 8608 in vibration analysis. *Journal of Testing and Evaluation*, 2017, 46(1): 405–418.
[32] A Sharkawy. Fuzzy and adaptive fuzzy control for the automobiles' active suspension system. *Vehicle System Dynamics*, 2005, 43(11): 795–806.
[33] L Guo, L Zhang. Robust H_∞ control of active vehicle suspension under non-stationary running. *Journal of Sound and Vibration*, 2012, 331(26): 5824–5837.
[34] L Yuan, H Zhao, H Chen, et al. Nonlinear MPC-based slip control for electric vehicles with vehicle safety constraints. *Mechatronics*, 2016, 38: 1–15.
[35] F Lin, P Shen. Robust fuzzy neural network sliding-mode control for two-axis motion control system. *IEEE Transactions on Industrial Electronics*, 2006, 53(4): 1209–1225.
[36] A J Tuononen, L Hartikainen, F Petry, et al. Parameterization of in-plane rigid ring tire model from instrumented vehicle measurements. *Proceedings of the 11th International Symposium on Advanced Vehicle Control*, Seoul, Korea. 2012: 9–12.

Ze Zhao is a PhD candidate at *School of Mechanical Engineering, Beijing Insitute of Technology, China*. His research interests include vehicle dynamics modelling and control.

Lei Zhang is a research professor at *School of Mechanical Engineering, Beijing Institute of Technology, China*. His research interests mainly lie in vehicle dynamics control and autonomous driving.

Xiaoling Ding is a research fellow at *Beijing Institute of Technology, China*. His research interests mainly lie in vehicle dynamics control.

Zhiqiang Zhang is a PhD candidate at *School of Mechanical Engineering, Beijing Institute of Technology, China*. His research interests include decision-making and motion planning for automated vehicles.

Shaohua Li is a professor at *Shijiazhuang Tiedao University, China*. Her research interests mainly lie in vehicle NVH analysis and vehicle dynamics control.

Liang Gu is a professor at *School of Mechanical Engineering, Beijing Institute of Technology, China*. His research interests mainly lie in vehicle NVH analysis and vehicle dynamics control.